

Tomographic imaging of resistive mode dynamics in the Madison Symmetric Torus reversed-field pinch

P. Franz, L. Marrelli, P. Piovesan, and I. Predebon

Consorzio RFX, Euratom-ENEA Association, Corso Stati Uniti 4, 35127 Padova, Italy

F. Bonomo

*Consorzio RFX, Euratom-ENEA Association, Corso Stati Uniti 4, 35127 Padova, Italy
and Department of Physics, University of Padova, via 8 Febbraio, 2-35122 Padova, Italy*

L. Frassinetti^{a)}

Consorzio RFX, Euratom-ENEA Association, Corso Stati Uniti 4, 35127 Padova, Italy

P. Martin

*Consorzio RFX, Euratom-ENEA Association, Corso Stati Uniti 4, 35127 Padova, Italy
and Department of Physics, University of Padova, via 8 Febbraio, 2-35122 Padova, Italy*

G. Spizzo

Consorzio RFX, Euratom-ENEA Association, Corso Stati Uniti 4, 35127 Padova, Italy

B. E. Chapman

Department of Physics, University of Wisconsin-Madison, 1150 University Avenue, Madison, Wisconsin 53706

D. Craig and J. S. Sarff

Department of Physics, University of Wisconsin-Madison, and NSF Center for Magnetic Self-Organization in Laboratory and Astrophysical Plasmas,^{b)} 1150 University Avenue, Madison, Wisconsin 53706

(Received 8 August 2005; accepted 1 December 2005; published online 25 January 2006)

A detailed study of the dynamics and magnetic topological effects of resistive-tearing modes is presented for different operational regimes in the Madison Symmetric Torus reversed-field pinch [R. N. Dexter *et al.*, *Fusion Technol.* **19**, 131 (1991)]. Soft-x-ray tomography and magnetic measurements, along with numerical reconstruction of magnetic-field lines with the ORBIT code [R. B. White and M. S. Chance, *Phys. Fluids* **27**, 2455 (1984)], have been employed. Magnetic-mode dynamics has been investigated in standard plasmas during the transition to the quasi-single helicity state, in which a single mode dominates the mode spectrum. Single helical soft-x-ray structures are studied with tomography in these cases. These structures are associated with magnetic islands, indicating that helical flux surfaces appear in the plasma. Mode dynamics has also been examined during auxiliary inductive current drive, the goal of which is to reduce the tearing-mode amplitudes. In this case the phenomenology of the soft-x-ray structures appearing in the plasma is more complex. In fact, when a quasi-single helicity spectrum occurs, a single island bigger than in the standard case is usually found. On the other hand, when all modes decrease, two helical soft-x-ray structures are observed, with the same helicity as the two innermost resonant modes. This constitutes the first direct evidence of magnetic-chaos reduction during auxiliary inductive current drive, which is responsible for the achievement of the best confinement in the reversed-field pinch configuration up to now. © 2006 American Institute of Physics.

[DOI: [10.1063/1.2160519](https://doi.org/10.1063/1.2160519)]

I. INTRODUCTION

Magnetohydrodynamic (MHD) instabilities in the core of magnetized fusion plasmas often play a significant role in determining their performance and, in general, their dynamical evolution.^{1,2} For a given instability, its impact on the plasma can be rather different: while moderate-sized sawtooth activity in the tokamak might be useful to avoid central impurity accumulation and remove fusion ash, in certain conditions sawteeth can produce seed islands, which trigger

performance-limiting neoclassical tearing modes. In the reversed-field pinch (RFP), resistive instabilities are needed to produce the dynamo electric field, which helps to sustain the configuration.³⁻⁸ But, if they are too many and too strong, they might spoil confinement. Many of the issues concerning the dynamics of MHD resistive instabilities in fusion plasmas are still unresolved. Therefore their accurate diagnosis continues to be necessary. This paper deals with the imaging of MHD resistive modes in the RFP configuration and aims both at providing a complete overview of their evolution in a variety of operational regimes and at contributing to the wide database of information on MHD instabilities in fusion devices.

^{a)}Present address: National Institute of Advanced Industrial Science and Technology (AIST), 1-1-1 Umezono, Tsukuba, Ibaraki 305-8568, Japan.

^{b)}URL: www.cmso.info.

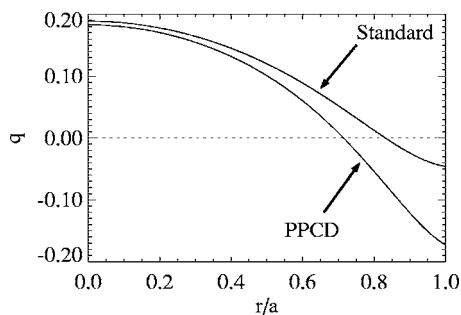


FIG. 1. Typical safety factor profiles for standard and PPCD MST discharges.

The RFP is a toroidal configuration for the magnetic confinement of thermonuclear plasmas.^{7,8} The RFP magnetic field has poloidal and toroidal components, B_θ and B_ϕ , respectively, which are generated not only through external coils, but also by electric currents flowing in the plasma, which cannot be sustained by a uniform toroidal induction electric field alone. The inductively driven electric field adds to a dynamo electric field, which is the result of a magnetic self-organization process resulting from the nonlinear interaction of resistive instabilities. Due to its relatively low safety factor $q(r) = rB_\phi(r)/[R_0B_\theta(r)]$, shown, for example, in Fig. 1, the RFP exhibits a rich magnetic spectrum, with modes resonant at several locations throughout the plasma. The poloidal and toroidal mode numbers of the largest amplitude modes are $m=0$ with low n and $m=1$ with $n \geq 2R_0/a$, where R_0 and a are the major and minor radii of the torus, respectively. It is worth noting that ideal nonresonant modes could also play an important role in the RFP dynamo process, as has been shown by recent numerical studies.⁹ Nevertheless, their effects seem not to be significant in the experiments considered in this work, where most of the dynamo is driven by resonant resistive instabilities.

In its simplest theoretical form, the RFP dynamo is produced by an individual resistive instability resonant in the plasma core, with poloidal mode number $m=1$ and toroidal mode number $n_0 \approx 2R_0/a$, hence the name single-helicity (SH) dynamo.^{10–13} This $m=1$ instability produces a helical perturbation of the magnetic field, which couples to a plasma velocity field due to an electrostatic drift.¹⁴ At the opposite extreme is the multiple-helicity (MH) dynamo, where the required electric field is produced by many nonlinearly interacting $m=1$ resistive instabilities.¹⁵ The effect on plasma performance of MH and SH spectra are very different. The MH dynamo is turbulent in nature. The spectrum of $m=0$ and $m=1$ modes in the plasma is very rich, and the overlap of the magnetic islands associated with them causes a broad region of stochastic magnetic field, with degraded particle and energy confinement. Magnetic-flux generation in MH states often happens in discrete and sudden dynamo events called sawtooth crashes.^{16,17}

The SH dynamo, on the opposite, is laminar in nature and preserves helical closed flux surfaces in the plasma core. In the SH regime, confinement could be strongly improved with respect to the standard MH state.¹⁸ Pure SH states have not yet been observed in experiments. However, hints of a

possible tendency of the plasma to relax toward them come from the experimental quasi-SH (QSH) states, where the spectrum of $m=1$ modes condenses spontaneously toward one dominant mode with a well defined toroidal number. QSH spectra have been observed in several RFP devices.^{19–24} Unlike the theoretical predictions, however, a superposition of secondary modes, i.e., modes with $m=1$ and $n > n_0$, remains. This does not allow the full performance of SH and maintains a stochastic magnetic field over a part of the plasma volume. Confinement in the QSH regime is improved in fact only within the helical coherent structure produced by the dominant mode.^{18,19} Experimental work aimed at finding the conditions which might facilitate the transition to pure SH states is on-going.²²

Lacking an experimental SH state, up to now the best results in terms of magnetic chaos healing have been obtained with the so-called pulsed poloidal current drive (PPCD) technique,²⁵ where a transient poloidal, or parallel, electric field is inductively driven in the plasma. Record low values of magnetic fluctuations and thermal transport have been obtained with PPCD in several RFPs.^{26–30} The highest electron temperature $T_e \approx 1300$ eV and the longest energy confinement time $\tau_E \approx 10$ ms in the RFP have been both achieved by means of this technique.^{31,32}

The RFP therefore provides several operational scenarios characterized by a very different structure of MHD instabilities, both in terms of their spectrum and amplitude. In this paper we present the results of a project aimed at imaging MHD resistive instabilities and characterizing their experimental properties in the RFP. This study relies heavily on a high-resolution x-ray tomography system,³³ which has been installed on the Madison Symmetric Torus (MST) device.³⁴ MST is a RFP with major radius $R_0=1.5$ m and minor radius $a=0.51$ m, characterized by a first wall which acts as both a close-fitting shell and toroidal field winding. The experiments described in this paper are characterized by a plasma current $I_p \approx 400$ kA and electron density $n_e \approx 1 \times 10^{19}$ m⁻³. A detailed analysis will be reported of single and multiple magnetic islands associated with different types of mode spectra, both in standard and PPCD operation, and their impact on magnetic chaos.

The paper is organized as follows. In Sec. II the tomography diagnostic system is described. In Sec. III the basic evidence of the existence of single soft-x-ray (SXR) islands is shown. In particular, the techniques used to detect, reconstruct, and simulate them are described. The identification of helical SXR structures with magnetic islands is also discussed. A statistical survey of the islands emerging during the sawtooth cycle of standard discharges is reported in Sec. IV, while the properties of islands during enhanced confinement PPCD plasmas are described in Sec. V, where evidence is given of the simultaneous emergence of multiple helical flux surfaces. A thorough comparison of tomographic reconstructions with Poincaré sections of the magnetic-field lines obtained with the code ORBIT is reported in Sec. VI, together with a final discussion on the relation between the emergence of helical SXR structures and magnetic-field topology.

II. THE MST TOMOGRAPHY SYSTEM

A study of the properties of MHD instabilities and their effects on the plasma requires knowledge of the perturbed magnetic topology. Direct measurements of the magnetic field by means of pickup coils are very useful, but generally limited to the plasma boundary. Laser Faraday rotation in MST provides line-integrated measurements of the equilibrium and fluctuating magnetic fields inside the plasma,³⁵ but a detailed characterization of internal magnetic fields would require an impractically high number of independent observations. For high-resolution mapping of nonuniform structures in magnetic-flux surfaces, measurement of the SXR emissivity spatial distributions is preferred.^{36–38} SXR tomography provides information on the magnetic field under some restrictive, but often verified, hypotheses. In fact, if the plasma can be described in the MHD framework, magnetic-flux surfaces are also surfaces of constant pressure. With high parallel transport, it is usually reasonable to assume that the electron density n_e and temperature T_e are also constant on the magnetic surfaces. The SXR emissivity is a strong function of n_e and T_e . Hence, iso-emissive surfaces are typically representative of magnetic-flux surfaces.

Tomography is the key technique for the reconstruction of the SXR emissivity. This is based on simultaneous multiple measurements of the SXR brightness $f(p, \phi)$, which is the emissivity function $\mathcal{E}(r, \theta)$ integrated along a line of sight $L(p, \phi)$:

$$f(p, \phi) = \int_{L(p, \phi)} \mathcal{E}(r, \theta) d\ell, \quad (1)$$

where p is the perpendicular distance from the line of sight to the center of the poloidal cross section and is called impact parameter; ϕ is the angle that the normal to the line of sight makes with the equatorial plane.

The measurements described in this paper have been made with a new SXR tomography system developed for MST.³³ SXR brightness is measured with two miniaturized pinhole cameras, each housing a linear array of silicon photodiodes. These act as radiation-to-current converters, with the output current proportional to the energy of the photons striking the detectors (3.6 eV is the value required to generate an electron-hole pair). Two fans of lines of sight, with a total of 24 channels, emanate from two pinholes at the plasma boundary. Beryllium foils of 16 μm thickness are placed on the pinholes and act as high-pass energy filters. The finite thickness of the diodes acts as a low-pass energy filter, so that the energy of the measured radiation ranges as a whole between about 1 and 7 keV. Curved beryllium foils are used, so that all the lines of sight view the plasma through the same foil thickness.

The probes are inserted through two 3.81-cm-diameter portholes located at the same toroidal position. In Fig. 2 a poloidal cross section of MST with the layout of the tomography lines of sight is shown. The SXR1 camera is located at 75° poloidal and mounted in a manipulator, which enables one to insert, extract, or rotate the diagnostic, and decouple it from the MST vacuum by means of a gate valve. The SXR2 camera is in a fixed position at 165° poloidal, without a gate

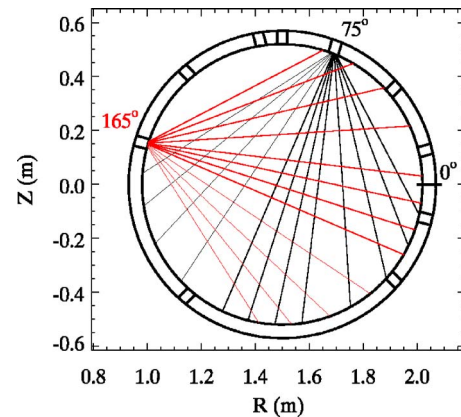


FIG. 2. (Color online). Chord geometry of the MST tomography. The two cameras are called SXR1 (black lines) and SXR2 (red lines). The detectors gather SXR radiation from 3D cones, whose axes are represented by the lines of sight in the figure.

valve. Signals are processed using both commercial and custom-made transimpedance linear amplifiers, with bandwidth ranging between 10 kHz for small signal levels typical of edge lines of sight and a few hundred kilohertz for higher signal levels, which are usually measured by lines of sight viewing the plasma core.

The relation between the current generated by the detectors and the SXR brightness is obtained by taking into account the finite diode and pinhole dimensions, which define a three-dimensional (3D) cone of sight. The photodiodes collect the SXR radiation emitted from the plasma volume inside each cone. In the poloidal cross section, the cones of sight of adjacent chords overlap by 50% and their axes are, by definition, the lines of sight, or chords, represented in Fig. 2. Assuming that the emissivity function has small variations in the direction orthogonal to the chords, the effect of the finite dimensions of the cones can be merged into a geometrical factor which is different for each line of sight and depends on the system detection geometry. Brightness profiles are therefore obtained from experimental data by dividing each current signal by the geometrical factor:

$$f_g = \frac{a_d a_{\text{ph}}}{4\pi d^2} \cos^4 \gamma, \quad (2)$$

where a_d is the detector area, a_{ph} the pinhole area, d the distance between the detector and pinhole planes, and γ the angle between the line of sight and the direction perpendicular to the detector plane.

In order to follow the rapid variations of SXR emissivity that may occur during a single shot, the diagnostic has been designed with a wide dynamic range. To illustrate these capabilities, in Fig. 3 the waveforms of plasma current I_p , electron density n_e , and surface electric field parallel to the equilibrium magnetic field $E_{\parallel}(a) = \mathbf{E} \cdot \mathbf{B} / B$ are shown along with the SXR brightness measured by a central chord for a typical PPCD shot. The period in which PPCD is applied is highlighted with a gray band, and the E_{\parallel} pulses associated with it are clearly seen. SXR emissivity strongly increases during PPCD, mainly reflecting an increase in electron temperature. Not only the central chords, but the whole radial brightness

profile is observed to increase during PPCD, as shown in Fig. 3(e) for three time instants during PPCD. Low-pass-filtered ($f < 3\text{ kHz}$) brightness profiles appear rather symmetric about the magnetic axis. A weak outward displacement is observed in the profiles measured by the SXR1 camera, which is located at a poloidal angle of 75° , and is thus sensitive to the Shafranov shift of the magnetic surfaces. In MST the magnetic axis is shifted outward of about 6 cm, while the last closed flux surface is shifted by a smaller amount, 1–2 cm, due to the close proximity of the plasma to the thick, close-fitting aluminum shell.

Measurements of the equilibrium magnetic field and its fluctuations (poloidal and toroidal components) have been made with a toroidal array of 32 magnetic coils located at the plasma boundary. This allows the detection of magnetic modes with toroidal mode number up to $|n|=15$.

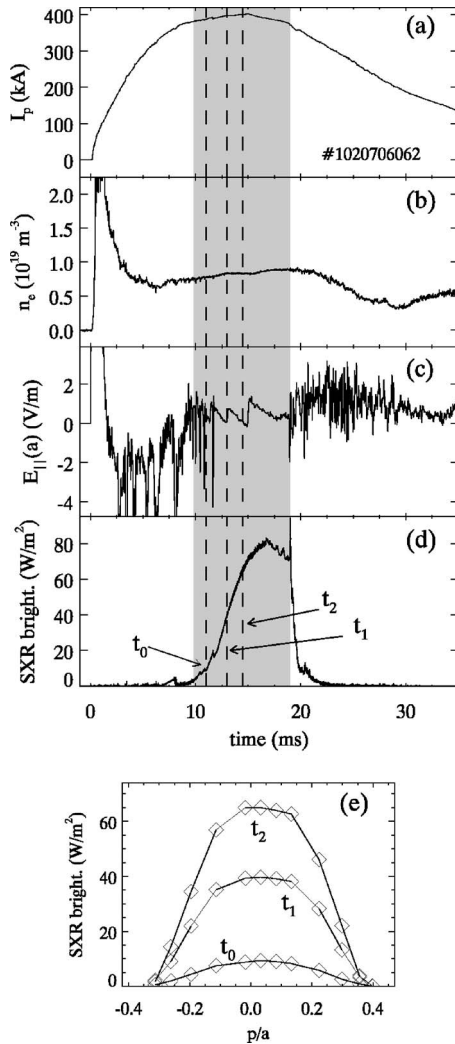


FIG. 3. Waveforms of the main plasma parameters for a PPCD discharge: (a) plasma current, (b) core electron density, (c) parallel electric field, and (d) core SXR brightness. The gray band highlights the period in which PPCD is applied. (e) Radial profiles of the SXR brightness at three times during PPCD.

III. THE IMAGING OF AN INDIVIDUAL HELICAL STRUCTURE

Tomographic reconstructions and mode rotation can be synergistically exploited to measure the detailed topological features of helical structures with a level of detail higher than in previous studies.^{38,39} This has been done by analyzing both tomograms of SXR emissivity and spatiotemporal fluctuation patterns of the brightness signals. A description of both approaches is given in the following sections.

A. Tomographic reconstructions of SXR emissivity

In the following we briefly review the Cormack method^{38,40–42} for tomographic reconstructions used in the present work. The Cormack approach solves Eq. (1) by using a Bessel-Fourier series expansion of the SXR brightness and emissivity functions. Due to the fact that helical structures are expected to be present in the plasmas studied here, the measured emissivity functions are usually more localized in Fourier space than in physical space, and this makes the Cormack technique preferable to others, such as the maximum-entropy-constrained finite-element algorithm or other hybrid methods.³⁸

In the Cormack approach, the brightness and emissivity functions are expanded in a truncated Fourier series due to the finite number of measurements:

$$f(p, \phi) = \sum_{m=0}^M [f_m^c(p) \cos(m\phi) + f_m^s(p) \sin(m\phi)], \quad (3)$$

$$\mathcal{E}(r, \theta) = \sum_{m=0}^M [\mathcal{E}_m^c(r) \cos(m\theta) + \mathcal{E}_m^s(r) \sin(m\theta)]. \quad (4)$$

Cormack proved that the following equation gives the integral relation between the Fourier components of (3) and (4):

$$\mathcal{E}_m^{c,s}(r) = -\frac{1}{\pi} \frac{d}{dr} \int_r^1 \frac{f_m^{c,s}(r) T_m(p/r) p dp}{p \sqrt{p^2 - r^2}}, \quad (5)$$

where $T_m(p/r)$ are the Tchebychev polynomials. As the tomographic problem is mathematically ill posed, the direct solution of (5) is not of practical use, because experimental noise can give rise to nonphysical spatial oscillations. Therefore, the Fourier components are usually radially expanded over a truncated set of Bessel functions,⁴² which are zero at the edge and do not require a regularization step as with the Zernicke polynomials. The integral relation (5) finally becomes a matrix equation:

$$\mathbf{f} = \mathbf{W} \cdot \mathcal{E}, \quad (6)$$

where the unknowns are the components of the so-called emissivity vector \mathcal{E} .

The arrangement of the lines of sight in the present work is such that poloidal harmonics up to $m=2$ can be resolved. As far as the radial dependence is concerned, the spacing and the number of lines of sight allow the first six terms of the expansion in the basis of Bessel functions to be determined. Depending on the particular profile being analyzed, these numbers may slightly change: they are typically optimized to

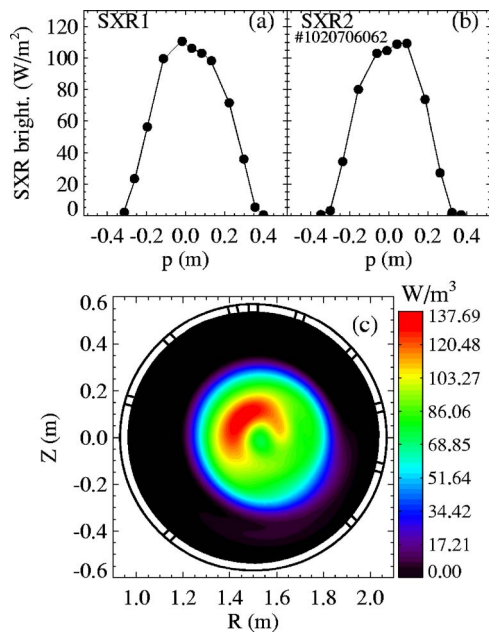


FIG. 4. (Color online). (a) and (b) SXR brightness profiles (full circles) with evidence of a radially localized structure. The data correspond to the same shot as in Fig. 3 at $t=15.47$ ms. The solid line represents the SXR brightness as computed from the inverted 2D emissivity map reported in (c), which shows the presence of a SXR island in the plasma core.

obtain smooth reconstructions. See Ref. 38 for details on the optimization of tomographic reconstruction and regularization techniques. Moreover, to increase the spatial resolution of the tomographic inversions, these are performed in the reference frame centered on the Shafranov-shifted magnetic axis.

An example of tomographic reconstruction during a PPCD discharge with a QSH spectrum is shown in Fig. 4 (this is the same discharge as in Fig. 3 and in Figs. 5–9). The brightness profiles used as inputs to the inversion algorithm are shown in Figs. 4(a) and 4(b) with full circles. The continuous line in these figures represents the brightness profiles computed from the inverted emissivity map. The matching between experimental and inverted data is very good. The reconstructed SXR emissivity map reported in Fig. 4(c) has a bean-shaped, highly emissive structure on top of a symmetric profile. A comparison with magnetic data shows that this structure is associated with the (1, 6) magnetic mode, which dominates the spectrum during QSH, as will be better shown in Fig. 5. The maximum SXR emissivity in the island is approximately 20% higher than the background emissivity. A detailed analysis of SXR coherent structures and their relation to magnetic measurements will be described in the next two sections by analyzing the spatiotemporal patterns of the brightness fluctuation signals.

B. Spatiotemporal SXR fluctuation patterns

The magnetic and SXR waveforms for the QSH PPCD discharge introduced in the previous section is shown in Fig. 5. The time evolution of the $m=1$, $n=6-9$ magnetic-mode amplitudes is reported in Fig. 5(a), where it is evident that

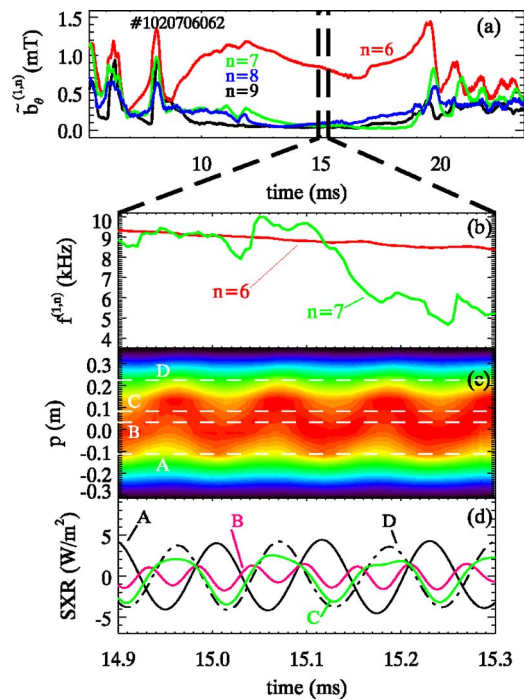


FIG. 5. (Color online). (a) Time evolution of the $m=1$, $n=6$ (red), $n=7$ (green), $n=8$ (blue), and $n=9$ (black) mode amplitudes for the same PPCD shot as in the previous figures. A transition to a QSH spectrum is observed to occur during PPCD. (b) Poloidal rotation frequency of the (1, 6) and (1, 7) modes. (c) Contour plot of the SXR brightness profiles measured by the SXR1 camera, which shows the presence of a rotating coherent structure in the plasma core. The horizontal dashed lines correspond to the lines of sight for which SXR signals are shown in (d).

the (1, 6) mode dominates over the others for a significant fraction of the discharge, and in particular, in the period when PPCD is applied, from 10 to 20 ms.

Regular oscillations are present in the brightness signals during QSH, with a frequency well correlated with the poloidal rotation frequency of the dominant (1, 6) magnetic mode, whose time evolution is shown in Fig. 5(b). The contour in Fig. 5(c) shows the time evolution of the brightness profile measured by the SXR1 camera. The maximum of the brightness profile oscillates around the magnetic axis of the plasma. This same oscillation is also evident in Fig. 5(d), in the brightness fluctuation signals corresponding to the chords from A to D, which are indicated with horizontal dashed lines in Fig. 5(c). The observed out-of-phase oscillation is produced by the rotation of an $m=1$ structure viewed by off-axis chords symmetric with respect to the center of the plasma column, for example, by chords A and D.

The fluctuation pattern becomes more complex when brightness signals measured by lines of sight passing near the magnetic axis are considered, as in chords B and C. A higher frequency component appears in these signals, which corresponds to the first harmonic of the (1, 6) mode poloidal rotation frequency. This is clearly visible on the signal measured by chord B and reported in Fig. 5(d). The appearance of this first harmonic will be explained below by means of a model of SXR emissivity. A similar frequency-doubling effect has been observed in many cases in tokamaks^{43,44} and also in previous RFP measurements.³⁷ In these cases the in-

terpretation of the frequency-doubling effect is analogous to that given here, being related to the rotation of a poloidally localized structure.

These same features can be found by analyzing the harmonic content of the SXR signals through the computation of wavelet spectra.⁴⁵ The wavelet spectra of the signals from chords B and D are shown in Fig. 6 and show two peaks at two distinct frequencies. In particular, the spectrum of the signal from the off-axis chord D shows a clear peak at the rotation frequency of the dominant (1, 6) mode and a weaker peak at its first harmonic. The spectrum of the signal from the central chord B in Fig. 6(b) instead displays a stronger peak at the first harmonic. A third peak corresponding to the second harmonic occasionally appears above the noise level. These frequencies decrease in time due to the mode breaking caused by the eddy currents induced in the conducting shell by the (1, 6) mode.⁴⁶

We show in the following that the fluctuation pattern described above is consistent with the presence of a radially and poloidally localized, helical SXR structure rotating in the laboratory frame. This has been verified with an emissivity model, which is illustrated in the following. SXR measurements are simulated by assuming that they are produced by a localized hot region added to an equilibrium emissivity profile and rotating at a constant angular velocity in flux surface coordinates. Toroidal effects are considered by assuming an outward differential shift of the equilibrium magnetic surfaces. In addition, the model also takes into account the helical displacement of the flux surfaces due to the dominant magnetic perturbation, as observed in RFX.³⁸ The model SXR emissivity of the island is given by the following formula:

$$\mathcal{E}(\rho, \theta, t) = \mathcal{E}_0 e^{-[\rho - \rho^*]^2 / \sigma_\rho^2} e^{-[\theta - \theta^*(t)]^2 / \sigma_\theta^2} + \mathcal{E}_1(\rho) \cos[\theta - \theta^*(t)]. \quad (7)$$

Here ρ is the flux surface radius, θ is the poloidal angle about

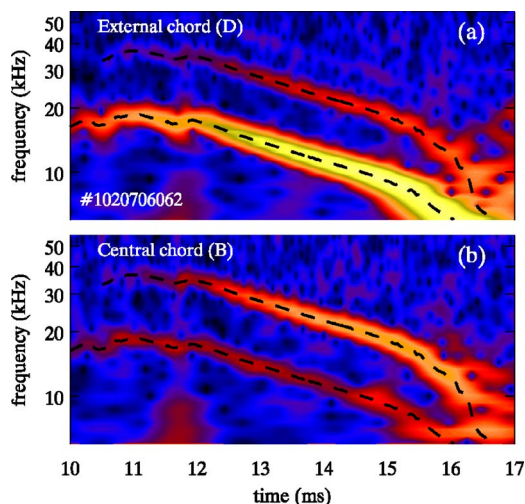


FIG. 6. (Color online). Wavelet spectra of the SXR brightness signals measured by (a) chord D and (b) chord C, as defined in Fig. 5. The dashed lines represent the poloidal rotation frequency of the dominant (1, 6) magnetic mode and its first harmonic.

the shifted magnetic axis, and ρ^* and θ^* are the radial and poloidal positions of the island, respectively. The equilibrium magnetic surfaces are assumed to have a circular cross section, with a differential displacement $\Delta(\rho) = \Delta_0(1 - (\rho/a)^2) + \Delta_h$, where $\Delta_0 = 6$ cm and $\Delta_h = 2.5$ cm. The first term in (7) describes the radial and poloidal shapes of the hotter region, which has been modeled with Gaussian functions of radial and poloidal widths σ_ρ and σ_θ , respectively. The second term includes the displacement of the plasma column due to a $m = 1$ helical magnetic perturbation. This occurs in the outer plasma region, i.e., for $\rho > \tilde{\rho} = \rho^* + 2\sigma_\rho$. The radial profile of $\mathcal{E}_1(\rho)$ is given by

$$\mathcal{E}_1(\rho) = \begin{cases} A(\rho/a)(1 - \rho/a), & \text{if } \rho > \tilde{\rho} \\ 0, & \text{if } \rho < \tilde{\rho}. \end{cases} \quad (8)$$

As the hot region rotates, the poloidal angle θ^* varies linearly with time, $\theta^*(t) = \theta_0 + 2\pi f^{(1,6)} t$, where $f^{(1,6)} = (R_0/6)v_\phi^{(1,6)}$ is the poloidal rotation frequency and $v_\phi^{(1,6)}$ is the toroidal velocity of the (1, 6) mode. The amplitudes \mathcal{E}_0 and \mathcal{E}_1 , radial position ρ^* , and widths σ_θ and σ_ρ of the Gaussian functions have been adjusted to match the experimental data. For the case shown in Figs. 5 and 6, a good agreement is obtained by assuming $\sigma_\theta \approx 0.3\pi$ and allowing the radial width to slightly vary with the poloidal angle $\theta^*(t)$ as follows: $\sigma_\rho(t) = \sigma_\rho^0 - 0.4 \cos[\theta^*(t)]$, where $\sigma_\rho^0 = 7.5$ cm. This implies that, in the polar coordinates (r, θ) , the difference in the size of the hot structure between the low-field side and the high-field side of the torus is bigger than the flux surface compression due to the differential shift.

In Fig. 7(a) a schematic of the model SXR island rotating in the poloidal cross section and the lines of sight previously shown in Fig. 5 are reported. The blue region in Fig. 7(a) represents the 90% contour level of the island emissivity at the time (1). The green circle represents the trajectory of the center of the rotating structure. The experimental brightness signals are displayed with black lines in Fig. 7(b) and the corresponding simulated signals are represented by red lines. The numbers in Fig. 7(b) highlight the peaks of the oscillation and correspond to the different positions, relative to the lines of sight, assumed by the structure during one poloidal turn.

In the framework of this model, the presence of the first harmonic in signals measured by central chords is explained as follows. Chords with impact parameter $p > \rho^*$ display a single peak, as the structure crosses the chord only once in a rotation period, e.g., position (1) for chord D and position (4) for chord A. Chords with $p < \rho^*$ are characterized by two peaks per period, as the region crosses them twice per rotation, e.g., positions (2) and (6) for chord C and positions (3) and (5) for chord B. The double-peak pattern, i.e., the higher harmonics in the central chords, is a necessary feature to account for the presence of a poloidally localized rotating structure, which has harmonic components with $m > 1$. In fact, when a sinusoidal poloidal dependence is assumed for the hot region, i.e., if the structure has a $m = 1$ component only, no signs of a double peak appear in the simulations. Several features of the SXR emissivity can be extracted directly from the fluctuating time series without performing a

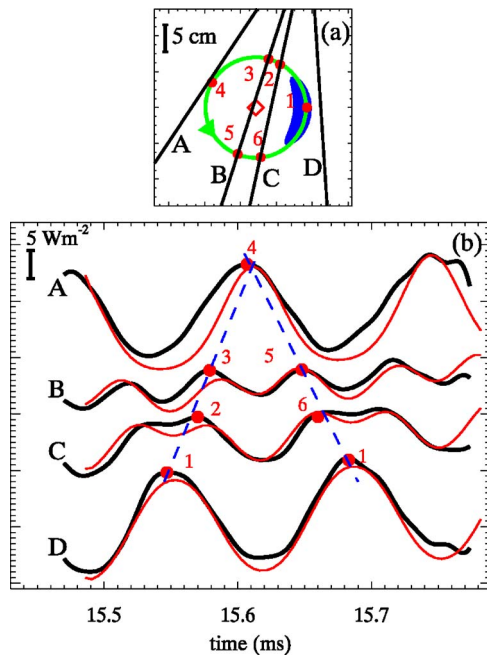


FIG. 7. (Color online). (a) Schematic of the SXR island used to model the experimental signals, as described in the text. The blue region corresponds to the 90% contour level of the model emissivity map. The chords from A to D are the same as in Fig. 5 and the diamond represents the magnetic axis. (b) Experimental (thick black line) and modeled (thin red line) high-pass-filtered SXR signals measured by the chords shown in (a). The numbers refer to the position of the SXR structure indicated in (a).

complete, but computing-time intensive, model fit. This feature will be extensively used in the next sections to detect the presence of helical structures directly from brightness signals.

It has been shown in Fig. 5 that SXR fluctuations measured by symmetric, off-axis chords have a phase delay close to π due to the rotation of the island structure. The exact value of this phase delay is due to the geometry of the lines of sight. In general, the phase delay between signals measured by two different chords A and B is $\Delta\phi = \phi_A - \phi_B$, where ϕ_A and ϕ_B are the chord impact angles. For two lines of sight parallel and opposite with respect to the rotation center, the phase delay would be $\Delta\phi = \pi$. In the case of a fan geometry, the phase delay is smaller and varies as a function of the impact parameter. For example, the radial profile of the phase delay with respect to chord A for the signals measured by the SXR1 probe is reported in Fig. 8. In particular, the phase delay between chords A and D is about 0.8π , as indicated with horizontal dotted lines. The solid line in the figure represents the phase delay computed from the modeled brightness signals, and a good agreement is found with the experimental data.

The instantaneous phase of an oscillation has been estimated with the Hilbert transform technique. It is assumed that each brightness signal $f(t)$ is given by the product of an instantaneous amplitude, also called envelope, $A(t)$ and the cosine of a phase function $\alpha(t)$. The functions $A(t)$ and $\alpha(t)$ can be computed through the Hilbert transform.⁴⁷ The advantage of the Hilbert transform with respect to standard coherence analysis is that, provided that a single oscillation is

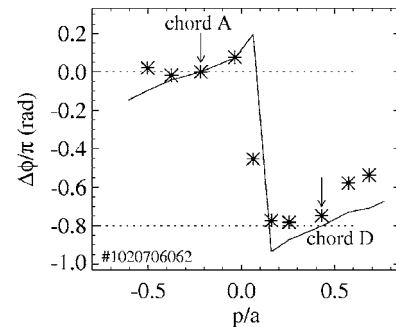


FIG. 8. Radial profile of the phase delay among signals measured by different chords at the dominant mode rotation frequency (stars). The phase delay is computed with the Hilbert analysis and is referred to chord A. The solid line represents the same phase delay calculated for the emissivity model described in the text.

present in the signal, its frequency and phase are determined more precisely even if they are slowly varying in time. The phase delay is finally obtained by time-averaging the difference of the phase functions of the brightness signals. The phase function is also a reliable indicator of the poloidal position of the magnetic island, $\theta^*(t) = \alpha(t) + \phi_0$, where ϕ_0 is the impact parameter of the line of sight.

The analysis of fluctuating SXR signals allows us to identify a rotating helical structure. If off-axis chords symmetric about the magnetic axis are characterized by a phase delay given by the difference of their impact parameters, and central chords display fluctuations at twice the dominant mode rotation frequency, then it can be concluded that a poloidally localized SXR structure rotates in the plasma core. These criteria can be applied automatically to large amounts of data. In fact, they will be used in the rest of the paper to identify the presence of SXR structures in large ensembles of discharges without performing mode complete, but also much more time consuming, tomographic reconstructions.

C. Identification of SXR structures with magnetic islands

Consistently with observations performed in the RFX experiment,^{19,22} the SXR structures detected in MST correspond to magnetic islands. In MST, due to magnetic-mode rotation, the identification of these structures can be performed on a single shot basis using fluctuation analysis. In fact, SXR islands are observed to rotate at the same frequency as the dominant magnetic modes. It has also been verified in several cases that the position of the highly emissive region corresponds to the magnetic island O point. It is shown in Fig. 9 that the position of the SXR structure $\theta^*(t)$, estimated with the Hilbert technique, corresponds to the poloidal position of the magnetic island O point, as derived from magnetic measurements. The toroidal array of pickup coils allows the determination of the amplitude and phase $\phi_n(t)$ of the poloidal component of the perturbed field. The poloidal position of the magnetic island O point $\theta^{\text{mag}}(t)$ corresponds to the position of maximum \tilde{b}_θ field taken at the same toroidal angle and is given by $\phi_n(t) + m\theta^{\text{mag}} + n\phi^{\text{toro}}$,

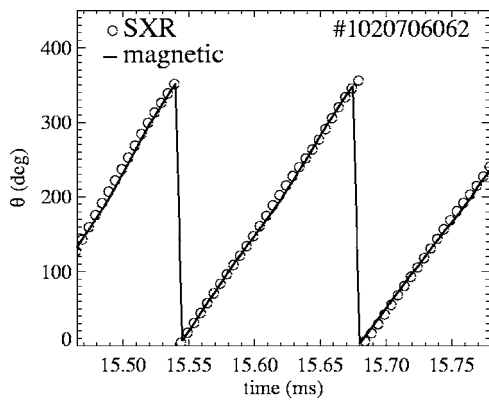


FIG. 9. Time evolution of the island poloidal position as computed from SXR fluctuation analysis (circles), compared with the poloidal position of the magnetic island O point as derived from magnetic measurements (line).

where $\theta^{\text{mag}}=241^\circ$ is the poloidal location of the toroidal array of pickup coils and $\phi^{\text{tomo}}=300^\circ$ is the toroidal location of the tomographic diagnostic.

As has already been pointed out, the SXR structure may theoretically be associated with the presence of a magnetic island. In fact, such an island may exist even if the amplitude of the secondary modes is not negligible.⁴⁸ To this end, a comparison has been performed between emissivity maps and Poincaré plots of the magnetic field as reconstructed by the Hamiltonian guiding-center code ORBIT (Refs. 18, 49, and 50) adapted to the RFP configuration.

The main characteristics of the model used to reconstruct the internal field topology are briefly recalled here. Experimental magnetic equilibria and perturbations are fed into the ORBIT code to reconstruct field maps or Poincaré plots. Equilibria are derived with the $\alpha-\Theta_0$ model,⁸ keeping the experimental values of the so-called reversal and pinch

parameters, $F=B_\phi(a)/\langle B_\phi \rangle$ and $\Theta=B_\theta(a)/\langle B_\theta \rangle$, respectively, as boundary conditions (here $\langle B_\phi \rangle$ is the toroidal magnetic field averaged over the poloidal cross section). The radial profile of the perturbations is obtained by solving the Newcomb equation⁵¹ in the zero-pressure approximation, for the specific equilibrium and for each (m,n) mode, with the experimental mode spectrum at the wall as a boundary condition.

Two examples of a comparison between tomographic reconstructions and Poincaré plots of the magnetic field are shown in Fig. 10. These are taken from standard MST discharges at $I_p \approx 400$ kA and correspond to different $m=1$ mode spectra. The bean-shaped structures appearing in Figs. 10(a) and 10(c) are characterized by different helicities, consistent with magnetic fluctuation analysis. In the first case the SXR structure rotates synchronously with the $(1,6)$ mode and the plasma is in a QSH state, while in the second case it corresponds to the $(1,5)$ mode during a MH state. The radial positions of the SXR structures and those of the corresponding magnetic island closely match. In particular, the radial position of the $(1,5)$ structure is more internal than the $(1,6)$ structure, as can be more precisely observed in Fig. 11. This depends on the shape of the q profile for which the $(1,5)$ resonance is more internal than the $(1,6)$, as will be better shown in the next section in Fig. 14.

It can thus be concluded that helical SXR structures closely correspond to magnetic islands. Having described the basic tools employed to identify thermal and magnetic islands, we now proceed to a systematic survey of different experimental regimes in MST to study the relation between resistive mode dynamics and the occurrence of magnetic islands.

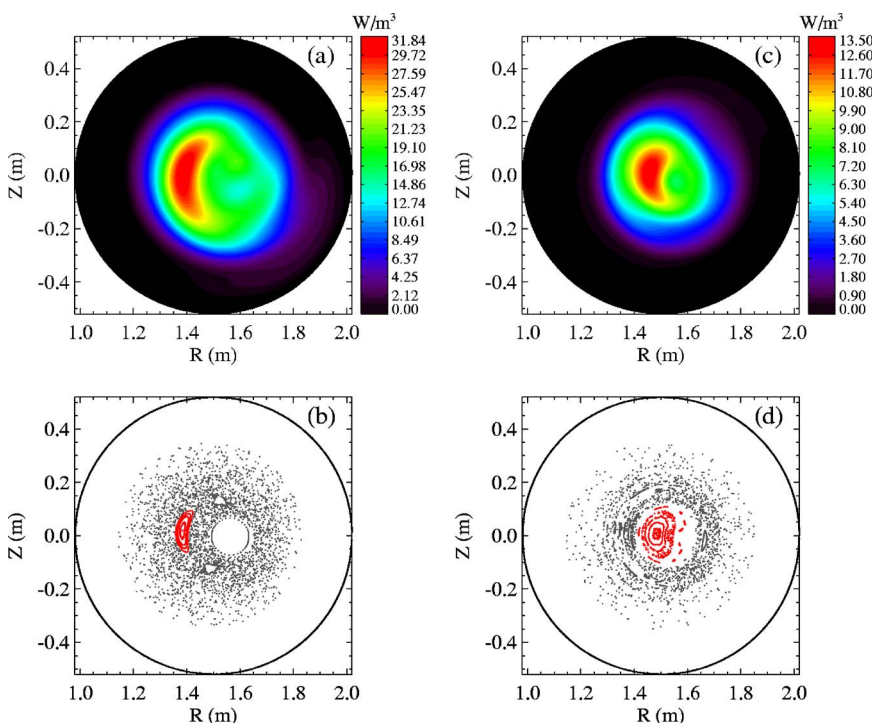


FIG. 10. (Color online). (a) Tomographic reconstruction of the SXR emissivity and (b) Poincaré plot of the magnetic-field lines from the ORBIT code for a $(1,6)$ island during a QSH state in a standard shot (No. 1020709059). (c) and (d) The same plots for a $(1,5)$ island during a MH state in a standard shot (No. 1020716054). The red points in the Poincaré plots indicate conserved flux surfaces.

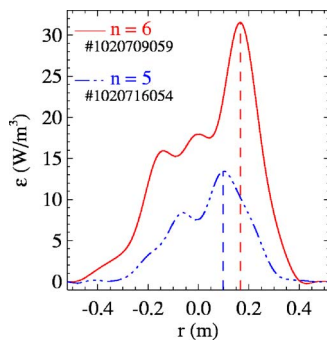


FIG. 11. (Color online). Radial profiles of the SXR emissivity for the two tomographic reconstructions of Fig. 10. The two radial profiles correspond to islands at the same poloidal position.

IV. IMAGING THE SAWTOOTH CYCLE OF STANDARD PLASMAS

As introduced in Sec. I, the standard RFP configuration is maintained in part via a self-organization process, which relies on the spontaneous excitation of $m=0, 1$ resistive modes. In MST a strong, turbulent dynamo activity mainly concentrates on discrete quasiperiodic events called sawteeth. In Fig. 12 the time evolution of the $m=1, n=5-12$ mode amplitudes and that of the core brightness is shown during a sawtooth cycle. In this example the amplitudes of modes with $n \neq 6$ grow rapidly at the sawtooth crash when the toroidal flux is also regenerated. A crash in the SXR signal occurs simultaneously as a consequence of the high level of magnetic stochasticity produced by the overlapping of islands associated with the broad spectrum of modes.

In this section, the dynamics of magnetic modes during the sawtooth cycle will be studied. It will be shown that the emergence of hot helical structures and the corresponding conserved flux surfaces is not a unique feature of QSH regimes. In fact, we will see that under particular conditions SXR helical structures appear also in the MH regime.

A group of about 100 similar discharges has been included in the present analysis, for a total of 399 sawtooth events. All these shots are characterized by a plasma current

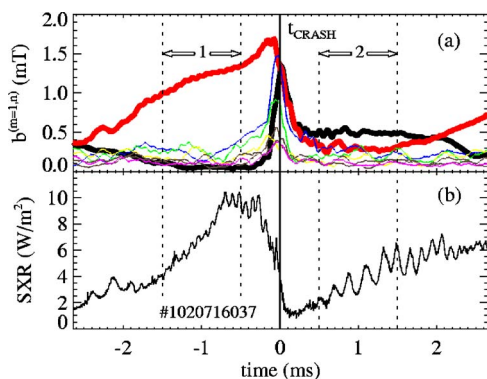


FIG. 12. (Color online). (a) Time evolution of the $m=1, n=5-12$ mode amplitudes and (b) of the core SXR brightness across a sawtooth crash in a standard shot. The $(1, 5)$ and $(1, 6)$ mode amplitudes are represented with thick black and red lines, respectively. The time $t=0$ ms corresponds to the sawtooth crash and the time intervals indicated with 1 and 2 are those used to build the precrash and postcrash ensembles described in the text.

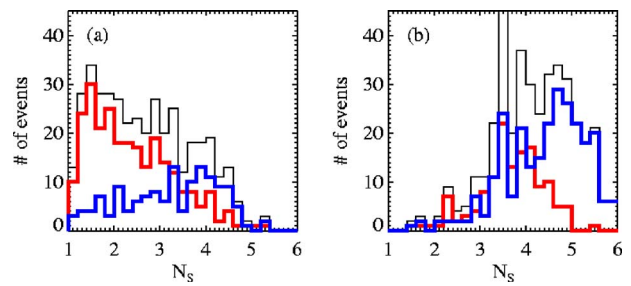


FIG. 13. (Color online). Histograms of N_S values for (a) the precrash and (b) postcrash ensembles. The black lines represent histograms of all events (399). The histogram of rotating events are represented by red lines: in 260 events the modes rotate before a sawtooth crash, while they are wall-locked in only 137 events after a crash. The histograms of wall-locked events are represented by blue lines. Before a crash, 33% of the events have a QSH spectrum, and in particular, 42% of the rotating events and 15% of the wall-locked ones. After a crash, only 1.5% of all the events have a QSH spectrum.

$I_p \approx 400$ kA, electron density $n_e \approx 1 \times 10^{19} \text{ m}^{-3}$, and reversal parameter $F \approx -0.2$. Two databases have been built: the first one includes the time periods just before a sawtooth crash (interval 1 in Fig. 12, from -1.5 to -0.5 ms, taking the crash time as $t=0$), while the second one includes the time periods which follow a crash (interval 2 in Fig. 12, from 0.5 to 1.5 ms). In these periods the equilibrium is nearly stationary and the plasma can either exist in a QSH or MH state.

Mode dynamics in QSH and MH states between sawtooth crashes is rather reproducible: the $(1, 6)$ dominant mode amplitude steadily increases in QSH, while all the modes have rather stationary amplitudes in MH. To define quantitatively a QSH or a MH state, the spectral spread number $N_S = [\sum_n (W_n / \sum_n W_n)^2]^{-1}$ is used, where $W_n = \tilde{b}_\theta^{(1,n)^2} / 2\mu_0$ is the magnetic energy of the $(1, n)$ mode.⁵² For low values of N_S , the energy is concentrated in the dominant modes: in the theoretical SH case the index value is exactly 1, while in the MH case it is of the order of the number of modes in the spectrum. Previous analyses have shown that a threshold value $N_S < 2$ is suitable to identify a QSH spectrum.²² The MH spectrum is defined as that with $N_S > 2$.

The statistical analysis of the distributions of the N_S spectral index for the precrash and postcrash ensembles are shown in Figs. 13(a) and 13(b), respectively (black line). While almost all the events in the postcrash ensemble have a MH magnetic spectrum, as shown also for a single shot in Fig. 12, a significant fraction of precrash events is characterized by a QSH spectrum. It is interesting to note that the probability of obtaining a QSH spectrum is also associated with the mode rotation velocity. To this end, the N_S distributions of periods with rotating (red line) and wall-locked (blue line) modes have been separated. During the precrash interval, plasmas with rotating modes have a higher probability of having a QSH spectrum, $P_{\text{QSH}} \approx 42\%$, than plasmas with wall-locked modes for which $P_{\text{QSH}} \approx 15\%$. This is consistent with theoretical models and experimental observations that MH plasmas are more likely to develop a rapid mode breaking.^{53,54} Based on this evidence only, a causal statement cannot be performed, i.e., we cannot state whether mode ro-

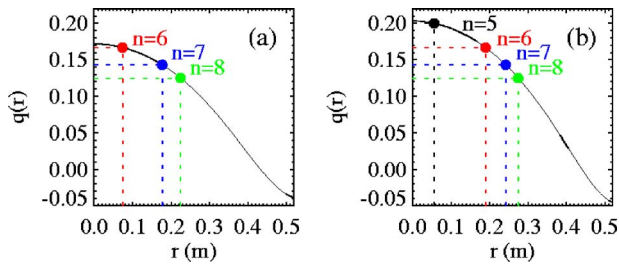


FIG. 14. (Color online). Safety factor profiles averaged over (a) the precrash and (b) postcrash ensembles. The dashed lines indicate the position of the resonant radii of the $(1, n)$ modes.

tation affects QSH occurrence or if this somehow favors rotation. The situation is rather different for the postcrash interval: QSH is rarely observed soon after a sawtooth crash. Moreover, while the $(1, 5)$ mode is never dominant before the sawtooth crash, and the $(1, 6)$ mode is dominant in 90% of the events, after the crash the $(1, 5)$ mode has the highest amplitude in 50% of the events. This phenomenology is consistent with the increase of the on-axis safety factor $q(0)$ following the sawtooth crash, as has been shown in Fig. 14 using the $\alpha-\Theta_0$ equilibrium model. After the crash, in fact, the $q=1/5$ resonant surface appears in the plasma, while before the crash the $(1, 5)$ mode should not be resonant.

The detection of SXR helical structures for all the events in the precrash and postcrash ensembles is based on the technique described in Sec. III. As explained before, a poloidally localized SXR island can be detected by the simultaneous presence of two indications: (i) a 0.8π phase shift between two opposite lines of sight and (ii) a significant amplitude of the first harmonic of the mode rotation frequency in the brightness signal measured by central lines of sight. Both of these quantities have been time-averaged in 1-ms-long periods in the precrash and postcrash ensembles. Only events with sufficiently high emissivity, $\mathcal{E} > 2 \text{ W/m}^2$, and with rotating modes have been selected for this analysis. Figure 15 reports the amplitude of the first harmonic as a function of the phase shift for the precrash and postcrash ensembles. QSH and MH periods, as defined by the N_S value, are separated. In the precrash ensemble, it is possible to distinguish two different regions, as shown in Fig. 15(a). The first one is

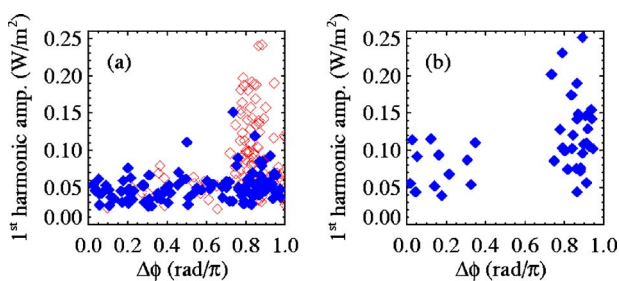


FIG. 15. (Color online). Distribution of the first harmonic amplitude for an on-axis line of sight as a function of the phase shift $\Delta\phi$ between two symmetric off-axis lines of sight at the dominant mode rotation frequency. The blue diamonds represent MH events and red open diamonds represent QSH events. (a) and (b) report, respectively, precrash and postcrash events. Only events with a SXR brightness greater than 2 W/m^2 and with mode rotation are included.

composed of MH periods (blue diamonds) and is a horizontal strip with low first-harmonic amplitude but increasing phase shift. This implies that a $m=1$ oscillation of the plasma column is sometime detected, but a poloidally localized helical structure is never present.

The second region is composed of QSH periods (red diamonds) and is a vertical strip with a phase shift of about 0.8π and a significant first-harmonic amplitude. Considering the events with $\Delta\phi \approx 0.8\pi$ and with a significant first-harmonic amplitude, or in other terms those which have a poloidally localized island, it is observed that 84% of them have a QSH spectrum. This is fully consistent with the picture of a thermal structure associated with helical flux surfaces accompanying a dominant mode in the magnetic spectrum. The fact that $\Delta\phi$ assumes values in the range from 0 to 0.8π , even during QSH when a helical structure is expected, is probably due to electromagnetic noise, which can be important if the signals are low.

The same analysis is reported in Fig. 15(b) for the postcrash ensemble. This reveals that in MST the picture is actually more complex than initially expected: an individual island can be present not only during QSH, but also with a MH spectrum. In fact, in the postcrash ensemble all the events correspond to a MH spectrum. The number of events is lower than for the precrash case, because of the requirement for a sufficiently high SXR emissivity, which is usually rather low soon after a crash. Even if all the $m=1$ modes have similar amplitude during these events, nearly 50% of them have a SXR structure and the brightness fluctuations are coherent with that of the $(1, 5)$ magnetic mode.

This phenomenology can be explained considering the time evolution of the magnetic equilibrium and the mode amplitudes across a sawtooth cycle. The magnetic island generated by the $(1, 5)$ mode is rather distant from the other resonant surfaces, as can be noted from the resonant radius of this mode in Fig. 14, and the mode amplitudes are relatively low. As a result, the overlap with other magnetic islands is reduced and helical $(1, 5)$ magnetic surfaces emerge in the core. This explanation is also confirmed by the comparison between the inverted emissivity map and the magnetic-field topology computed by the ORBIT code, as was shown above in Figs. 10(b) and 10(d).

A statistical analysis of the brightness fluctuation patterns shows that the radial location of the $(1, 5)$ islands is more internal than for the $(1, 6)$ case. This confirms statistically what was shown above in the tomographic reconstruction of Fig. 10. Ensemble-averaged radial profiles of the SXR fluctuation amplitude, in a narrow frequency range around the rotation frequency of the dominant mode and of its first harmonic, are reported in Figs. 16(a) and 16(b), respectively. The average has been performed only over events for which a SXR structure is present, i.e., $(1, 6)$ in the precrash period and $(1, 5)$ in the postcrash period. The fluctuation amplitude profile of the dominant frequency shows two peaks, both for the precrash and postcrash cases. These correspond to the radii where the rotating islands are positioned. They are located in fact around the rational surfaces of the $(1, 5)$ and $(1, 6)$ modes, respectively, as reconstructed with the $\alpha-\Theta_0$ equilibrium model. The radial profiles of the first-

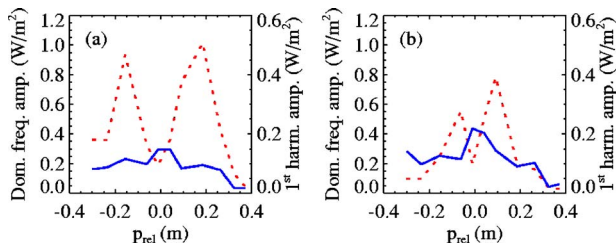


FIG. 16. (Color online). Average profiles of the SXR fluctuation amplitude at the dominant mode rotation frequency (red dashed line) and at its first harmonic (blue line) in (a) the precrash and (b) postcrash ensembles.

harmonic amplitude are peaked instead in the central region of the plasma. As previously explained, this is due to the fact that the SXR islands have not pure $m=1$ structure, but are poloidally localized.

V. IMAGING PULSED POLOIDAL CURRENT DRIVE PLASMAS

The appearance of helical SXR structures associated with magnetic islands has also been investigated during pulsed poloidal current drive (PPCD) experiments. Even for these cases it will be shown that the phenomenology of islands is far richer than previously observed. PPCD has been pioneered in MST as a mechanism to reduce the intrinsic, high level of magnetic fluctuations in the standard RFP.²⁸ As said in Sec. I, the final effect is an overall improvement of the confinement, with an increase of the core electron temperature by a factor of 2–3.³¹ Although the initial perturbation is applied at the plasma edge, the PPCD effect is global and takes place on the time scale typical of the MHD activity.^{31,55} In fact, when the E_{\parallel} pulses are applied, the magnetic-mode amplitude rapidly decreases. This implies that the change of the fields at the edge rapidly affects the mode eigenfunctions over the entire plasma radius.

The survival of a single $m=1$, n_0 mode to produce a QSH spectrum with very low amplitude secondary modes is a distinctive feature of a significant fraction of PPCD discharges in MST.²¹ An example was shown above in Figs. 3–9. In this case, the reduction of the secondary modes is contemporary to the growth of the (1, 6) dominant mode. A similar behavior has been found previously also in the RFX experiment.⁵⁶ Both MH and QSH spectra are actually observed during PPCD. Two such examples are reported in Fig. 17.

The dynamics of magnetic modes during PPCD determines the appearance of one or two structures in the SXR

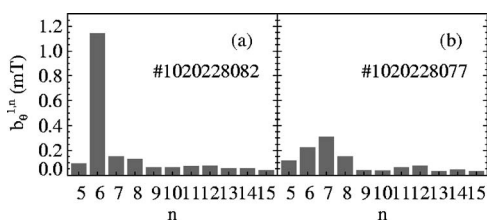


FIG. 17. Examples of toroidal-mode number spectra of $m=1$ modes for (a) a QSH and (b) a MH PPCD discharge.

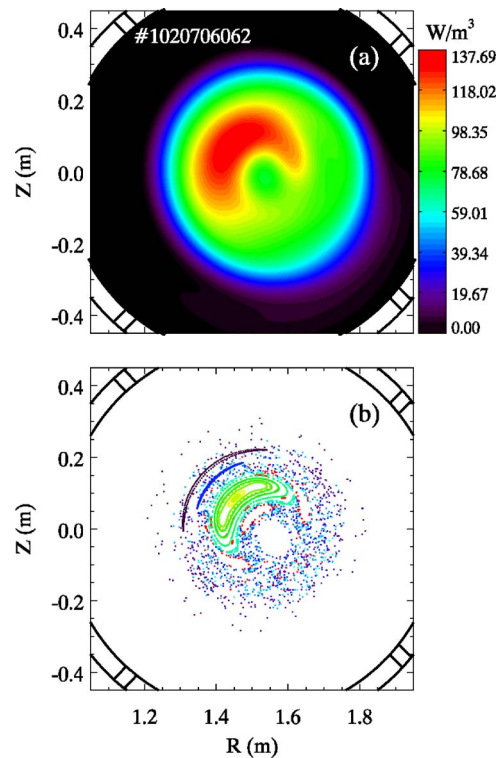


FIG. 18. (Color online). (a) SXR emissivity map reconstructed during the QSH PPCD discharge presented in Figs. 3–9. (b) ORBIT reconstruction of the magnetic-field lines at the same time instant.

tomogram, which are associated with QSH and MH spectra, respectively. The comparison of emissivity maps with ORBIT reconstructions allows us to state that both cases are signatures of a strong magnetic turbulence reduction.³⁹ In fact, a fundamental ingredient of successful PPCD operation is the *strong decrease of the secondary, $n \neq n_0$ modes*, which results in a reduction of the overall magnetic stochasticity in the core. This is also confirmed by recent measurements of energetic electrons during PPCD.⁵⁷

A. Imaging of the QSH PPCD: The emergence of single helical flux surfaces

When an individual $m=1$ mode dominates the mode spectrum during PPCD, a single, bean-shaped structure appears in the plasma core and rotates at the poloidal frequency $f^{(1,6)}$ of the dominant (1, 6) mode, similarly to what happens in standard QSH plasmas. The phenomenology of brightness fluctuation signals, with the oscillations at the frequency $f^{(1,6)}$ and the presence of its first harmonic $2f^{(1,6)}$, is in all respects similar to that already discussed in Sec. III for standard discharges. In Fig. 18(a) a tomographic reconstruction of a bean-like structure is displayed. The structure stretches over a significant fraction of the plasma radius and is rather elongated in the poloidal direction: the 80% iso-emissive contour covers a poloidal angle of about 200° . A Poincaré plot performed with the ORBIT code for the same shot and time instant is shown in Fig. 18(b). The region with conserved flux surfaces resembles, both in radial and poloidal extensions, the SXR structure of Fig. 18(a).

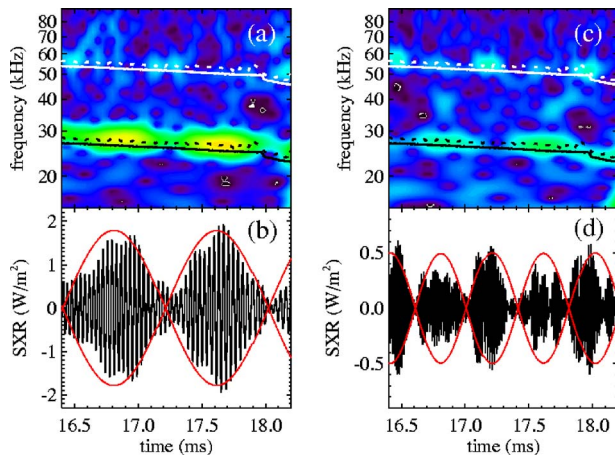


FIG. 19. (Color online). (a) Wavelet of the SXR signal shown in (b), which is measured by an off-axis chord during a MH PPCD discharge and band-pass filtered around the rotation frequency of the (1, 6) and (1, 7) modes. (c) and (d) are the same as (a) and (b), respectively, but for a central chord. The mode frequencies $f^{(1,6)}$ and $f^{(1,7)}$ are represented on the wavelet contours by black solid and dashed lines, respectively. The white lines correspond to the first harmonic of these two frequencies.

With a procedure similar to that described in Sec. III, we can identify the bean-shaped structure of Fig. 18(a) with the magnetic island, which arises at the resonance of the (1, 6) mode. Both the SXR and the magnetic islands during PPCD are bigger than similar structures occurring in standard plasmas. This is mainly due to the reduction of secondary mode amplitudes and is a general feature of PPCD experiments with a QSH spectrum.

B. Imaging of the MH PPCD: The emergence of multiple helical flux surfaces

As discussed at the beginning of this section, the appearance of a rotating double SXR structure is characteristic of MH PPCD plasmas when two modes with similar, low amplitudes are present in the plasma core. Low amplitudes are associated with small islands, which in turn determine small spatial changes in SXR signals. For this reason, SXR measurements of multiple coherent structures are more difficult to perform than for single helical structures. Evidence of the presence of two islands in the core of MST has been recently found, starting from analysis of brightness fluctuation patterns.³⁹

An example of SXR signals during a PPCD discharge with multiple structures is shown in Fig. 19. The shot corresponds to a case with similar (1, 6) and (1, 7) mode amplitudes and rotation frequencies. The two modes rotate at similar but not identical frequencies $f^{(1,6)}$ and $f^{(1,7)}$. The slight difference induces a beat pattern in the fluctuating component of the SXR signals, as shown in Fig. 19(b) for an edge chord (signals are band-pass filtered around the dominant frequency, $f \approx 27$ kHz). The high-frequency oscillation corresponds to the average frequency of the (1, 6) and (1, 7) mode amplitudes, while the envelope corresponds to the frequency of the beating structure, which is given by $\hat{f} = f^{(1,7)} - f^{(1,6)}$. The wavelet spectrum of Fig. 19(a) also shows the

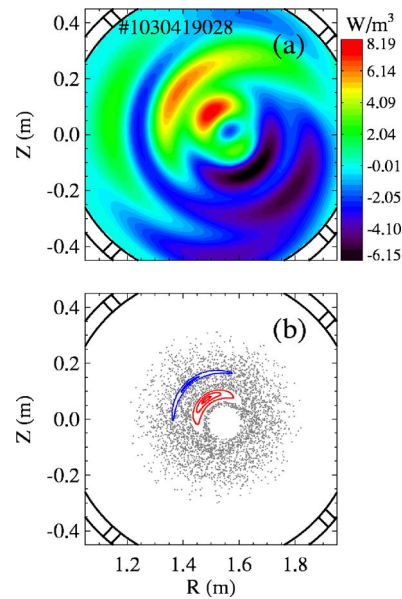


FIG. 20. (Color online). (a) SXR emissivity map reconstructed from high-pass-filtered signals and (b) ORBIT reconstruction of the magnetic-field lines during a MH PPCD discharge in which the (1, 6) and (1, 7) islands appear simultaneously.

presence of the beating at the mode rotation frequency. The overplotted solid and dashed lines represent the frequencies of the two modes.

The analysis of the filtered SXR signal measured by a central chord is reported in Figs. 19(c) and 19(d) and gives the key evidence for the simultaneous presence of two islands. In fact, a beating pattern at the frequency of the first harmonic is also present. In this case the band-pass filter is around the frequency of the first harmonic, between 30 and 50 kHz. Since SXR oscillations at the first-harmonic frequency imply the presence of a *single*, poloidally localized helical structure, the beat at that frequency implies that *two* such structures are present in the plasma core. PPCD shots with small amplitudes of the innermost (1, 6) and (1, 7) modes are characterized by the presence of two individual, small (1, 6) and (1, 7) islands.³⁹

The above result is also confirmed by the tomographic reconstruction shown in Fig. 20(a). This has been performed considering only the fluctuating component of the measured brightness signals, so that the radial shape of the perturbed emissivity is better visualized. These signals have been filtered between 22 and 64 kHz to retain also the first harmonic of the fluctuation. The radial positions of the two structures are consistent with the resonance radii of the (1, 6) and (1, 7) modes. By analyzing a sequence of tomographic reconstructions, not shown here, the two structures rotate in the poloidal direction at different velocities, the difference in the poloidal angle being $\Delta\theta = \theta^{(1,6)} - \theta^{(1,7)} = 2\pi\hat{f}t$.

The field line tracing performed with the ORBIT code and reported in Fig. 20(b) shows the presence of two magnetic islands at the same radial positions of the reconstructed SXR structures. A 3D reconstruction of the conserved helical flux surfaces through the ORBIT code is also reported in Fig. 21.⁵⁸

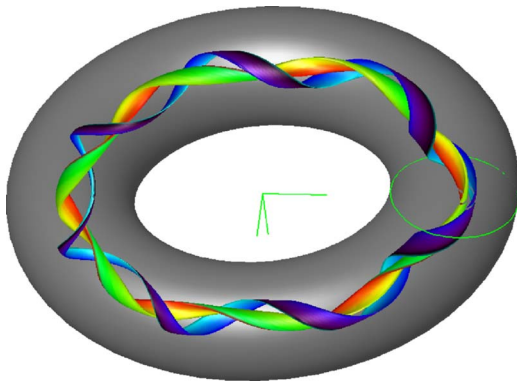


FIG. 21. (Color online). 3D reconstruction from the ORBIT code of the magnetic surfaces corresponding to the (1, 6) and (1, 7) islands during a MH PPCD discharge. The green circle indicates the poloidal plane corresponding to the Poincaré section shown in Fig. 20(b).

VI. DISCUSSION AND CONCLUSIONS

In MST helical SXR structures are present both in standard and PPCD plasmas. These thermal structures have been mapped by means of SXR tomography and identified with $m=1$, n magnetic islands. It has been shown that thermal islands appear not only in plasmas with a QSH spectrum, but also during MH regimes. In standard plasmas a (1, 5) island can form soon after the sawtooth crash, when the plasma has typically a MH magnetic spectrum. This is explained by the fact that the on-axis safety factor $q(0)$ increases above $1/5$ after a crash, the resonant surfaces are quite separated, and all the mode amplitudes are low enough that island overlap is suppressed. PPCD plasmas, on the other hand, can have both a QSH spectrum with the presence of a single SXR island or a MH spectrum characterized by the appearance of multiple islands. This is the first observation of multiple structures in a RFP and it is caused by the strong magnetic-mode reduction produced by PPCD.

The presence and size of thermal islands do not depend only on the dominant mode amplitude, but also on the average amplitude of the secondary modes, as has already been pointed out theoretically. In fact, when the mode amplitudes are comparable, magnetic chaos is produced by the island-overlap mechanism. On the other hand, when the dominant mode amplitude is much higher than the neighboring ones in QSH states, the classical resonance overlap criterion no longer applies. In these cases the expulsion of the island separatrix has been suggested as a mechanism for explaining the emergence of helical flux surfaces out of a stochastic background.⁴⁸

To obtain a more quantitative and comprehensive description of this phenomenon, a series of similar standard and PPCD shots with $I_p \approx 400$ kA has been analyzed, looking for the presence of SXR islands by means of the techniques described in Sec. III. The experimental magnetic spectrum changed from shot to shot. Here the amplitudes of the two innermost resonant modes, i.e., the (1, 6) and (1, 7) modes, are considered. In these shots the (1, 7) mode amplitude is roughly proportional to the average amplitude of the secondary modes; therefore the decrease of the (1, 7) is on average simultaneous to a decrease of all the other modes. In

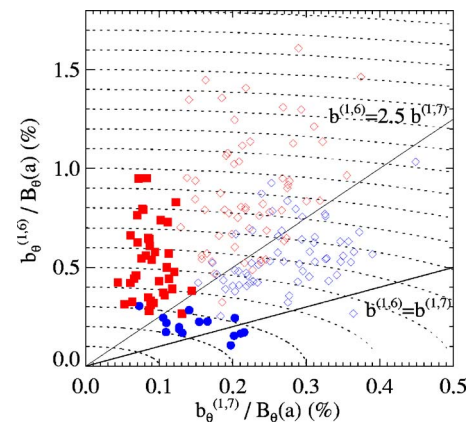


FIG. 22. (Color online). Normalized amplitude of the two innermost resonant (1, 6) and (1, 7) modes for several, similar standard and PPCD discharges. The data refer to PPCD discharges in which single (red filled squares) or double (blue filled circles) SXR islands are observed in tomographic reconstructions. The red and blue open diamonds indicate QSH and MH states from precrash periods in standard shots, respectively. The dashed lines indicate loci of constant-mode energy.

Fig. 22 the normalized amplitude of these modes for standard precrash periods (open symbols) and PPCD plasmas (full symbols) are reported. The different symbols also indicate whether one (red diamonds for standard QSH and red squares for PPCD QSH), two (blue circles), or no (blue diamonds) SXR islands are present in the plasma. The figure suggests that, independent of the operating conditions, i.e., standard discharges in the precrash phase or PPCD discharges, reaching a lower threshold value for the ratio $\bar{b}^{(1,6)}/\bar{b}^{(1,7)}$ is a necessary condition for a (1, 6) SXR island to appear. This extends a result obtained in the past for PPCD shots.³⁹ Moreover, two islands can simultaneously be present only during PPCD discharges with a MH mode spectrum, when all the mode amplitudes are sufficiently low, while no structures emerge in standard MH plasmas.

To explain the behavior of the islands described above for the experiment, the dependence of the magnetic island widths computed by ORBIT on the magnetic spectrum has been analyzed. We have considered a simplified model spectrum (see the inset of Fig. 23 for an example) in which the (1, 6) and (1, 7) mode amplitudes have been varied in a rather wide range. The amplitude of the modes with $n > 7$ is multiplied by the same factor as the (1, 7) mode, since in the experiment the average amplitude of these secondary modes is proportional to that of the (1, 7) mode, as said above. For each value of the normalized (1, 6) and (1, 7) mode amplitudes, the radial width of the respective magnetic islands have been determined from the Poincaré plots. The width of the (1, 6) island is represented by the contour in Fig. 23 as a function of $\bar{b}_\theta^{(1,6)}/B_\theta(a)$ and $\bar{b}_\theta^{(1,7)}/B_\theta(a)$.

Despite the simplified model spectrum, the dependence of the (1, 6) island width on the mode amplitudes is rather complex. The presence of the (1, 7) mode is the first limiting factor to the (1, 6) island width, as the (1, 7) island overlaps with the (1, 6) one. In particular, for low values of the normalized (1, 7) mode amplitude, i.e., for $\bar{b}_\theta^{(1,7)}/B_\theta(a) < 0.15\%$, the (1, 6) island width is a growing function of the

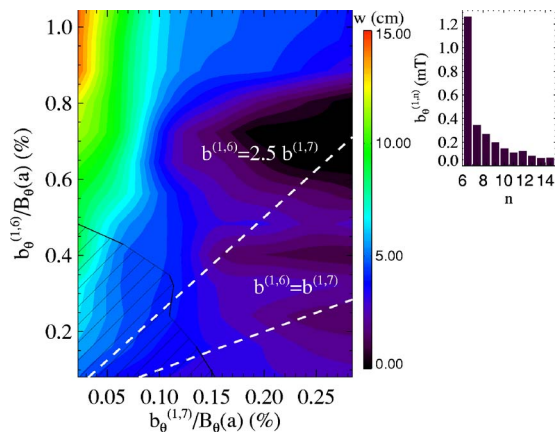


FIG. 23. (Color online). (a) The (1, 6) island width as a function of the normalized (1, 6) and (1, 7) mode amplitudes. All island widths are computed for the same equilibrium, only modifying the magnetic spectrum shown in (b) by rescaling independently the amplitude of the dominant and of all the secondary modes. The dashed region indicates values of the mode amplitudes for which a (1, 7) island emerges with a radial width greater than 1 cm.

mode amplitude, even if a simple dependence like $w^{(1,6)} \propto \sqrt{\tilde{b}_{\theta}^{(1,6)}}$, which is predicted for a linearly unstable tearing mode, does not hold. Similarly to what is observed in the experiment, islands bigger than 3 cm are found when $\tilde{b}_{\theta}^{(1,6)}/\tilde{b}_{\theta}^{(1,7)}$ exceeds a value of about 2.5.

When both the (1, 6) and (1, 7) mode amplitudes are low enough, two islands are observed to appear in the Poincaré plots, which have the same helicity as these modes. A (1, 7) island of radial width $w^{(1,7)} > 1$ cm is found for values of the mode amplitudes in the shaded region of the figure. When the $\tilde{b}_{\theta}^{(1,7)}/B_{\theta}(a)$ mode amplitude is higher, and consequently, all the other secondary mode amplitudes are higher, no (1, 7) island appears.

This model can give only qualitative information, because of the simplified spectrum used. In particular, the island dimensions for standard discharges may differ from the corresponding values of the figure due to the slightly different shape of the secondary-mode spectrum. Moreover, the equilibrium magnetic-field profile of standard discharges is different from the one used in the model, which can affect systematically the position and width of the island. Nonetheless, the simplified model used to reconstruct the island widths qualitatively reproduces the general behavior of Fig. 22, and in particular, (i) the presence of a (1, 6) island when the ratio between the two innermost resonant-mode amplitudes is greater than 2.5; (ii) the presence of at least two islands when $\tilde{b}_{\theta}^{(1,6)} \approx \tilde{b}_{\theta}^{(1,7)}$ and both mode amplitudes are below 0.2%, i.e., in the MH PPCD case; and (iii) the absence of islands when $\tilde{b}_{\theta}^{(1,6)} \approx \tilde{b}_{\theta}^{(1,7)}$ with both amplitudes sufficiently large, i.e., in MH standard discharges.

In summary, the emergence of helical flux surfaces out of a chaotic magnetic field is a complex phenomenon that depends on many factors, including magnetic equilibrium and details of the spectrum. Nonetheless, the ratio of the innermost resonant modes measured at the edge gives indications on the presence of one or two islands in the case

considered here. The investigation of the mechanism of magnetic surface destruction and restoration related to the overlap of magnetic islands, together with the experimental observation of SXR islands in the core of MST, allows us to provide the first direct evidence of magnetic chaos reduction both in QSH periods and, more dramatically, during PPCD experiments. The observed reduction of mode energy measured at the edge occurs throughout the whole plasma and the modeling of eigenfunctions is confirmed by the experimental observation of hot SXR structures.

ACKNOWLEDGMENTS

The authors would like to gratefully acknowledge the technical contribution of M. Reyfmann. The RFX people thank the MST team for the useful discussions and continuous support. The authors also acknowledge stimulating discussions with S. C. Prager and D. F. Escande.

This work was supported by the European Communities under the contract of Association between EURATOM/ENEA. The views and opinions expressed herein do not necessarily reflect those of the European Commission.

- ¹G. Bateman, *MHD Instabilities* (MIT, Cambridge, MA, 1978).
- ²J. P. Freidberg, *Ideal Magnetohydrodynamics* (Plenum, New York, 1987).
- ³H. A. B. Bodin and A. A. Newton, *Nucl. Fusion* **20**, 1255 (1980).
- ⁴R. G. Watt and R. A. Nebel, *Phys. Fluids* **26**, 1168 (1983).
- ⁵D. D. Schnack, E. J. Caramana, and R. A. Nebel, *Phys. Fluids* **28**, 321 (1985).
- ⁶V. Antoni, P. Martin, and S. Ortolani, *Nucl. Fusion* **29**, 1759 (1989).
- ⁷H. A. B. Bodin, *Nucl. Fusion* **30**, 1717 (1990).
- ⁸S. Ortolani and D. D. Schnack, *Magnetohydrodynamics of Plasma Relaxation* (World Scientific, Singapore, 1993).
- ⁹S. Cappello, *Plasma Phys. Controlled Fusion* **46**, B313 (2004).
- ¹⁰S. Cappello and R. Paccagnella, *Phys. Fluids B* **4**, 611 (1992).
- ¹¹J. M. Finn, R. A. Nebel, and C. C. Bathke, *Phys. Fluids B* **4**, 1262 (1992).
- ¹²D. F. Escande, S. Cappello, F. D'Angelo, P. Martin, S. Ortolani, and R. Paccagnella, *Plasma Phys. Controlled Fusion* **42**, B243 (2000).
- ¹³S. Cappello and D. F. Escande, *Phys. Rev. Lett.* **85**, 3838 (2000).
- ¹⁴D. Bonfiglio, S. Cappello, and D. F. Escande, *Phys. Rev. Lett.* **94**, 145001 (2005).
- ¹⁵D. J. Den Hartog, J. T. Chapman, D. Craig, G. Fiksel, P. W. Fontana, S. C. Prager, and J. S. Sarff, *Phys. Plasmas* **6**, 1813 (1999).
- ¹⁶S. Hokin, A. Almagri, S. Assadi *et al.*, *Phys. Fluids B* **3**, 2241 (1991).
- ¹⁷H. Ji, A. F. Almagri, S. C. Prager, and J. S. Sarff, *Phys. Rev. Lett.* **73**, 668 (1994).
- ¹⁸I. Predebon, L. Marrelli, P. Martin, and R. B. White, *Phys. Rev. Lett.* **93**, 145001 (2004).
- ¹⁹D. F. Escande, P. Martin, S. Ortolani *et al.*, *Phys. Rev. Lett.* **85**, 1662 (2000).
- ²⁰P. Martin, A. Buffa, S. Cappello *et al.*, *Phys. Plasmas* **7**, 1984 (2000).
- ²¹L. Marrelli, P. Martin, G. Spizzo *et al.*, *Phys. Plasmas* **9**, 2868 (2002).
- ²²P. Martin, L. Marrelli, G. Spizzo *et al.*, *Nucl. Fusion* **43**, 1855 (2003).
- ²³P. Piovesan, G. Spizzo, Y. Yagi, H. Koguchi, T. Shimada, Y. Hirano, and P. Martin, *Phys. Plasmas* **11**, 151 (2004).
- ²⁴P. Piovesan, D. Craig, L. Marrelli, S. Cappello, and P. Martin, *Phys. Rev. Lett.* **93**, 235001 (2004).
- ²⁵J. S. Sarff, S. A. Hokin, H. Ji, S. C. Prager, and C. R. Sovinec, *Phys. Rev. Lett.* **72**, 3670 (1994).
- ²⁶R. Bartiromo, P. Martin, S. Martini *et al.*, *Phys. Rev. Lett.* **82**, 1462 (1999).
- ²⁷Y. Yagi, Y. Maejima, H. Sakakita, Y. Hirano, H. Koguchi, T. Shimada, and S. Sekine, *Plasma Phys. Controlled Fusion* **44**, 335 (2002).
- ²⁸J. S. Sarff, J. K. Anderson, T. M. Biewer *et al.*, *Plasma Phys. Controlled Fusion* **45**, A457 (2003).
- ²⁹M. Cecconello, J.-A. Malmberg, G. Spizzo *et al.*, *Plasma Phys. Controlled Fusion* **46**, 145 (2004).
- ³⁰L. Frassinetti, Y. Yagi, H. Koguchi, T. Shimada, and Y. Hirano, *Phys. Plasmas* **11**, 5229 (2004).

- ³¹B. E. Chapman, J. K. Anderson, T. M. Biewer *et al.*, Phys. Rev. Lett. **87**, 205001 (2001).
- ³²B. E. Chapman, A. F. Almagri, J. K. Anderson *et al.*, Phys. Plasmas **9**, 2061 (2002).
- ³³P. Franz, G. Gadani, R. Pasqualotto *et al.*, Rev. Sci. Instrum. **74**, 2152 (2003).
- ³⁴R. N. Dexter, D. W. Kerst, T. W. Lovell, S. C. Prager, and J. C. Sprott, Fusion Technol. **19**, 131 (1991).
- ³⁵D. L. Brower, W. X. Ding, S. D. Terry *et al.*, Rev. Sci. Instrum. **74**, 1534 (2003).
- ³⁶G. A. Wurden, Phys. Fluids **27**, 551 (1984).
- ³⁷G. Chartas and S. Hokin, Phys. Fluids B **4**, 4019 (1992).
- ³⁸P. Franz, L. Marrelli, A. Murari, G. Spizzo, and P. Martin, Nucl. Fusion **41**, 695 (2001).
- ³⁹P. Franz, L. Marrelli, P. Piovesan *et al.*, Phys. Rev. Lett. **92**, 125001 (2004).
- ⁴⁰A. M. Cormack, J. Appl. Phys. **34**, 2722 (1963).
- ⁴¹A. M. Cormack, J. Appl. Phys. **35**, 2908 (1964).
- ⁴²L. Wang and R. S. Granetz, Rev. Sci. Instrum. **62**, 1115 (1991).
- ⁴³J. A. Wesson, Nucl. Fusion **29**, 641 (1989).
- ⁴⁴P. C. de Vries, G. Waidmann, A. Krämer-Flecken, A. J. H. Donné, and F. C. Schüller, Plasma Phys. Controlled Fusion **39**, 439 (1997).
- ⁴⁵C. Torres and G. P. Compo, Bull. Am. Meteorol. Soc. **79**, 61 (1998).
- ⁴⁶B. E. Chapman, R. Fitzpatrick, D. Craig, P. Martin, and G. Spizzo, Phys. Plasmas **11**, 2156 (2004).
- ⁴⁷J. S. Bendat and A. G. Piersol, *Random Data: Analysis and Measurement Procedures* (Wiley, New York, 2000).
- ⁴⁸D. F. Escande, R. Paccagnella, S. Cappello, C. Marchetto, and F. D'Angelo, Phys. Rev. Lett. **85**, 3169 (2000).
- ⁴⁹R. B. White and M. S. Chance, Phys. Fluids **27**, 2455 (1984).
- ⁵⁰R. B. White, *Theory of Toroidally Confined Plasmas* (North Holland Physics, Amsterdam, 1989).
- ⁵¹D. C. Robinson, Nucl. Fusion **18**, 939 (1978).
- ⁵²Y. L. Ho, D. D. Schnack, P. Nordlund, S. Mazur, H.-E. Satherblom, J. Scheffel, and J. R. Drake, Phys. Plasmas **2**, 3407 (1995).
- ⁵³D. J. Den Hartog, A. F. Almagri, J. T. Chapman, H. Ji, S. C. Prager, J. S. Sarff, R. J. Fonck, and C. C. Hegna, Phys. Plasmas **2**, 2281 (1995).
- ⁵⁴S. C. Guo and M. S. Chu, Phys. Plasmas **11**, 4050 (2004).
- ⁵⁵M. E. Puiatti, S. Cappello, R. Lorenzini *et al.*, Nucl. Fusion **43**, 1057 (2003).
- ⁵⁶A. Cravotta, G. Spizzo, D. Terranova *et al.*, Phys. Plasmas **10**, 705 (2003).
- ⁵⁷R. O'Connell, D. J. Den Hartog, C. B. Forest *et al.*, Phys. Rev. Lett. **91**, 045002 (2003).
- ⁵⁸F. Bonomo, B. E. Chapman, P. Franz *et al.*, IEEE Trans. Plasma Sci. **33**, 458 (2005).